CATALYSIS

Dynamic interplay between metal nanoparticles and oxide support under redox conditions

H. Frey[1,2]†, A. Beck[2,3]†, X. Huang[1,4]*, J. A. van Bokhoven[2,3]*, M. G. Willinger[1]*‡

The dynamic interactions between noble metal particles and reducible metal-oxide supports can depend on redox reactions with ambient gases. Transmission electron microscopy revealed that the strong metal-support interaction (SMSI)–induced encapsulation of platinum particles on titania observed under reducing conditions is lost once the system is exposed to a redox-reactive environment containing oxygen and hydrogen at a total pressure of ~1 bar. Destabilization of the metal–oxide interface and redox-mediated reconstructions of titania lead to particle dynamics and directed particle migration that depend on nanoparticle orientation. A static encapsulated SMSI state was reestablished when switching back to purely oxidizing conditions. This work highlights the difference between reactive and nonreactive states and demonstrates that manifestations of the metal-support interaction strongly depend on the chemical environment.

Noble metal nanoparticles (NPs) are used as active constituents of catalysts and thus play an important role in the sustainable production of chemicals and fuels and the mitigation of pollutants. The interesting catalytic properties of noble metals emerge when dispersed as nanometer-sized particles on high–surface area oxide supports. Although simple models attribute catalytic properties mainly to size effects, with the metal being the active phase on an inert oxide support, synergistic interactions between metal and support can be critical (*1*, *2*).

A prominent example of metal-support interactions is the loss of hydrogen chemisorption of titania-supported platinum (Pt–TiO_2) upon high-temperature reductive treatment (HTR). The effect, which was first observed by Tauster *et al*. (*3*), can be reverted through a series of high-temperature oxidation and subsequent low-temperature reduction steps (*3*). Originally, the chemisorption suppression was attributed to an electronic perturbation of the system, that is, the bonding between Pt and Ti cations under reducing atmospheres. Subsequent studies showed that in situ reductive activation leads to encapsulation of Pt NPs in a thin, partially reduced layer of TiO_2 (*4*–*10*). The driving force for this so-called strong metal-support interaction (SMSI) state was attributed to surface energy minimization (*11*).

Similar encapsulation effects have also been reported for Co (*12*), Ni (*13*, *14*), Au (*15*), and Cu (*16*) NPs. More recently, it was shown that high-temperature oxidative treatment can also lead to NP encapsulation (*15*, *17*–*20*). Potential benefits of SMSI encapsulation include enhanced resistivity against both NP coalescence and Ostwald ripening (*21*–*23*). Furthermore, the selectivity of the catalyst can be tuned by modifying the adsorption strength of molecules on the catalyst surface and by blocking specific active sites (*24*–*28*). Hence, the ability to exploit synergistic interactions between metal NPs and their support in a controlled way is of high interest with regard to the development of improved catalysts and processes.

Early studies on the SMSI were mostly based on indirect, integral spectroscopic observations and provided evidence of NP encapsulation either through an altered chemical composition of the surface or through SMSI-induced changes in the chemisorption capacity. High-resolution real-space methods, such as scanning tunneling microscopy (STM) and transmission electron microscopy (TEM), can provide direct atomic-scale imaging to confirm the formation of the encapsulating SMSI state after high-temperature reductive (*29*–*31*) or, respectively, oxidizing treatment (*4*). However, because of methodological constraints, direct imaging of the encapsulated state has mostly been achieved ex situ, in experiments in which the SMSI state was preserved during cooling and sample transfer from the catalytic reactor to the high-vacuum environment of a microscope. Despite detailed characterization of preserved SMSI states, little is known about metal-support interactions under catalytic reaction conditions.

Because the chemical states of metal particles and reducible support are influenced by the chemical environment (*32*, *33*), their mutual interaction and possible synergistic effects should be investigated under catalytic working conditions. Direct real-space observations by in situ STM and environmental TEM have shown gas-phase–induced reconstruction of NPs (*34*–*37*) and changes at the metal-support interface (*38*). Environmental TEM is generally limited to chamber pressures of ~20 mbar (*39*). Depending on the system studied, the pressure-dependent chemical potential of reactive species might thus be too low to trigger specific processes and reactions that are relevant for catalytic function at higher pressure. However, the development and commercial availability of microelectromechanical-based reactors for in situ electron microscopy has extended the accessible pressure range by roughly two orders of magnitude (*11*, *40*, *41*) and enabled partially bridging the so-called pressure gap (*42*).

This study builds on earlier investigations of interfacial dynamics on oxide-supported noble metal NPs (*38*, *43*, *44*). Working at higher pressure allows us to visualize gas phase–induced processes that are directly linked to metal-support interactions and revealed the dynamic interplay between NP, support, and gas phase under working conditions. We selected a Pt–TiO_2 catalyst because it is the archetype system for which the SMSI state was first described (*3*) and for which we have recently shown that a static encapsulated state of Pt NPs exists not only under hydrogen but also under purely oxidizing conditions, however, with a specific overlayer structure that depends on the gas environment (*4*). We studied hydrogen oxidation because it is the most elementary redox reaction that can also be viewed as a representation of many reactions, such as partial hydrocarbon oxidations. Furthermore, this catalytic system only yields water in gas phase reactions at high temperatures (*45*). Our in situ TEM-based study revealed how the classical encapsulated SMSI state of Pt can be lost through destabilization of the overlayer once the system is exposed to a redox-active regime in which H_2 and O_2 are simultaneously interacting with the catalyst.

Under reaction conditions, we observed interfacial dynamics that are characterized by local structural collapse and rebuilding of TiO_2, i.e., redox processes involving the reduction and subsequent reoxidation of the support underneath Pt NPs. In this process, the inherent lattice mismatch between Pt and TiO_2 and the associated interfacial strain lowers the barrier for vacancy formation in the reducible oxide. The resulting interfacial reconstructions give rise to pronounced changes in particle morphology and, eventually, particle mobility. Previous studies in which purely reducing or oxidizing environments were used did not show such dynamics and were not representative of reaction conditions (*4*, *11*, *46*, *47*). Water, which is formed as a reaction product, is not the cause of the observed phenomena. Instead, addition of water to the feed suppresses particle dynamics. Relevant for the NP behavior is the configuration of the metal-support interface, as

[1]Scientific Center of Optical and Electron Microscopy (ScopeM), ETH Zürich, 8093 Zürich, Switzerland. [2]Institute for Chemical and Bioengineering, ETH Zürich, 8093 Zürich, Switzerland. [3]Paul Scherrer Institute, 5232 Villigen, Switzerland. [4]College of Chemistry, Fuzhou University, Fuzhou 350116, P. R. China.
*Corresponding author. Email: xinghuang@fzu.edu.cn (X.H.); jeroen.vanbokhoven@chem.ethz.ch (J.A.vB.); marc.willinger@tum.de (M.G.W.)
†These authors contributed equally to this work.
‡Department of Chemistry, Technical University of Munich, Lichtenbergstrasse 4, D-85748 Garching, Germany.

shown for three selected cases of differently oriented NPs. This work provides an explanation for the observed particle restructuring and directed particle migration on the support. Furthermore, it provides additional evidence for a nonclassical SMSI state that is observed in oxidizing conditions (*17*, *20*, *48*).

Results

Switching to a redox-active H_2–O_2 mixture

We investigated the metal-support interactions and the relevance of an SMSI encapsulated state under redox conditions. TiO_2-supported Pt NPs were first heated in H_2 to induce the classical SMSI state and then transferred under inert gas purging into an O_2 atmosphere. As described in (*4*) and detailed in the experimental part (supporting materials and methods), this treatment led to Pt NPs in a nonclassical oxidized SMSI state. Once prepared, the system was transited into the relevant redox-reactive regime through addition of H_2 into the O_2 flow. This sequence led to a gradual change in the encapsulated state of the Pt NPs and, finally, complete removal of the overlayer (Fig. 1, A to F). The first observable effect that could be attributed to an increasing partial pressure of H_2 in the reactor was the onset of overlayer reduction. It was detected as an instant change in the overlayer structure on the (001) facet (movie S1), followed by retraction of the overlayer on the (111) plane (Fig. 1). The latter initiated near an uncovered Pt{110}-type microfacet, as indicated by the propagating reduction front in the image sequence of Fig. 1, G to I (see also movie S2). Within seconds, the overlayer vanished from the Pt{111} surfaces, whereas some transient patches, which selectively decorated Pt{100} planes, could still be observed (Fig. 1, C and D, and movies S1 and S2). Similar transiently existing nanopatches were observed for the Pt–TiO_2 system in field ion microscopy (*49*) and were reported for iron oxide–supported Pt NPs (*50*).

Once the gas composition reached a set mixture (60 mbar H_2 and 700 mbar O_2) after ~180 s, the encapsulating overgrowth layer was fully retracted from all particles. Thus, stable configurations of static Pt particles exhibiting encapsulating layers existed either in pure H_2 (the classical SMSI state) or in pure O_2 (the nonclassical SMSI state), but not in a regime in which both gases were simultaneously present. Signs of the structural incompatibility between the reduced and oxidized overlayers on the Pt particles could also be detected at the remaining NP-support interface (see next section). With the removal of the overlayer, Pt NPs furthermore underwent a shape change through a slight expansion of {100} facets (see Fig. 1, A, G, and F, and structure model in fig. S3). Once the overlayer was fully removed, the onset of pronounced particle dynamics involving restructuring and migration was observed (see image sequence in Fig. 1, E and F, and movie S1).

Particle and interfacial dynamics in the redox-active regime

Movies recorded at lower magnification showed the response of a collection of NPs to reaction conditions. As shown in movie S3, the degree of structural dynamics and mobility differed between NPs. Some NPs remained static, whereas others underwent structural fluctuations; some remained stationary, whereas others migrated across the substrate surface. These individual dynamics indicate that each NP responded according to local surface topological features and the configuration of the interface.

Because rutile TiO_2 preferentially exposes low-energy (110) facets (*51*) and Pt NPs were generally present in the form of truncated cuboctahedra, exposing mostly {100} and {111} facets, only a limited number of interface configurations need to be considered for a general description of the observed behavior. Indeed, a preferential orientation relationship between the Pt NP and the support is evident from the analysis of lattice fringes of isolated Pt NPs that are attached to the same TiO_2 particle. As shown in Fig. 2E and the corresponding colorized lattice fringes in the Fourier-filtered image in Fig. 2F and fig. S4, the particles show identical orientation of their (111) and (100) planes, and thus, preferential orientation driven by a minimization of the lattice misfit induced interfacial strain.

The first NP we considered (Fig. 2, A to C) was oriented with Pt(111) planes perpendicular to the Pt–TiO_2 interface. Images that were recorded after overlayer retraction showed occasional slight rotations of the NP. Such slight rotations could be induced by reconstructions at the interface, which is similar to the recently reported case of gas phase–induced rotation of gold NPs on a TiO_2 support, which was observed by low-pressure environmental TEM (*43*). With increasing H_2 partial pressure, the Pt NP developed pronounced structural dynamics that involved twin formation and shearing along Pt(111) planes in an up-down motion, perpendicular to the Pt–TiO_2 interface (see arrows in Fig. 2C). This up-down motion can be seen in Fig. 2D, which was generated by cutting a plane through the recorded image stack along the time axis, and is also shown in movie S4.

These structural dynamics at the interface imply that the TiO_2 substrate locally collapsed and at a later point in time was rebuilt. The

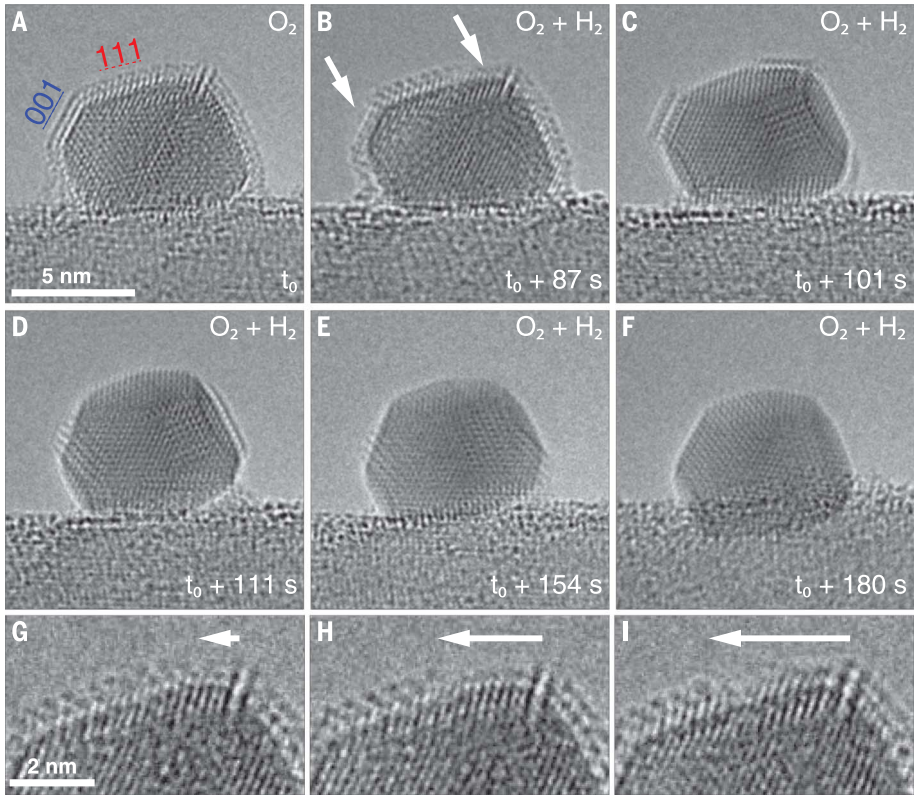

Fig. 1. Morphological change upon transition into the redox-active regime. (**A** to **F**) Images that were recorded while the composition of the gas phase in the in situ gas cell gradually changed from 700 mbar O_2 to a mixture of 60 mbar H_2 plus 700 mbar O_2. (**G** to **I**) Magnified images of the particle surface that show the gradual reduction of the overlayer between frames A and B. t_0 is the time at which the H_2 flow was turned on.

cross-sectional view provided by TEM imaging showed a substantial reshuffling of material at the interface, with Pt (111) planes moving up and down in response. Characteristic for this process is the pronounced formation of (111)-twinning planes, which has also been observed for the case of zinc oxide–supported copper NPs in a redox environment (*52*).

The second case, shown in Fig. 2, G to J, and movie S5, represents NPs in which Pt(111) planes were oriented almost parallel to the Pt–TiO_2 interface. Here, a repetitive forward-and-backward step flow–like motion of Pt{111} planes was observed. Similar to the case of Pt(111)-planes moving up- and downwards in Fig. 2, A to C, this motion could be caused by similar redox processes, however, rotated by 90° and without the involvement of twinning planes running through the Pt NP.

The third case we considered was a Pt NP oriented with a {001} plane parallel to the Pt–TiO_2 interface. Because TEM images only show a two-dimensional (2D) projection of a 3D object, the precise location of the interface was not clear in Fig. 2, K to N. Nevertheless, we could follow the shape evolution of the moving NP with time and abstract information about the ongoing processes. The NP exposed Pt(111) planes that were inclined with respect to the interface. At times, microfaceting of the (111) plane was observed at the right side of the particle, which, in effect, tilted it down toward the substrate (see Fig. 2K). Moments later, the right side reconstructed until a planar (111) facet was restored. This downward inclination and subsequent retraction occurred repetitively, whereas the opposing (111) plane on the left side, which faced away from the substrate, did not show any change. The reshuffling of Pt at one end was responsible for a net transport of Pt from the right (back side) to the left (front side) and resulted in a propagating motion. This redox chemistry–driven directional migration of the Pt NP is shown in movie S6.

These three cases show how the relative orientation of Pt NP and the TiO_2 support can be linked to the behavior of individual NPs. Depending on the configuration of the interface, the underlying redox processes can give rise either to Pt NPs that restructure and do not move or to NPs that restructure and migrate on the surface in a directed manner.

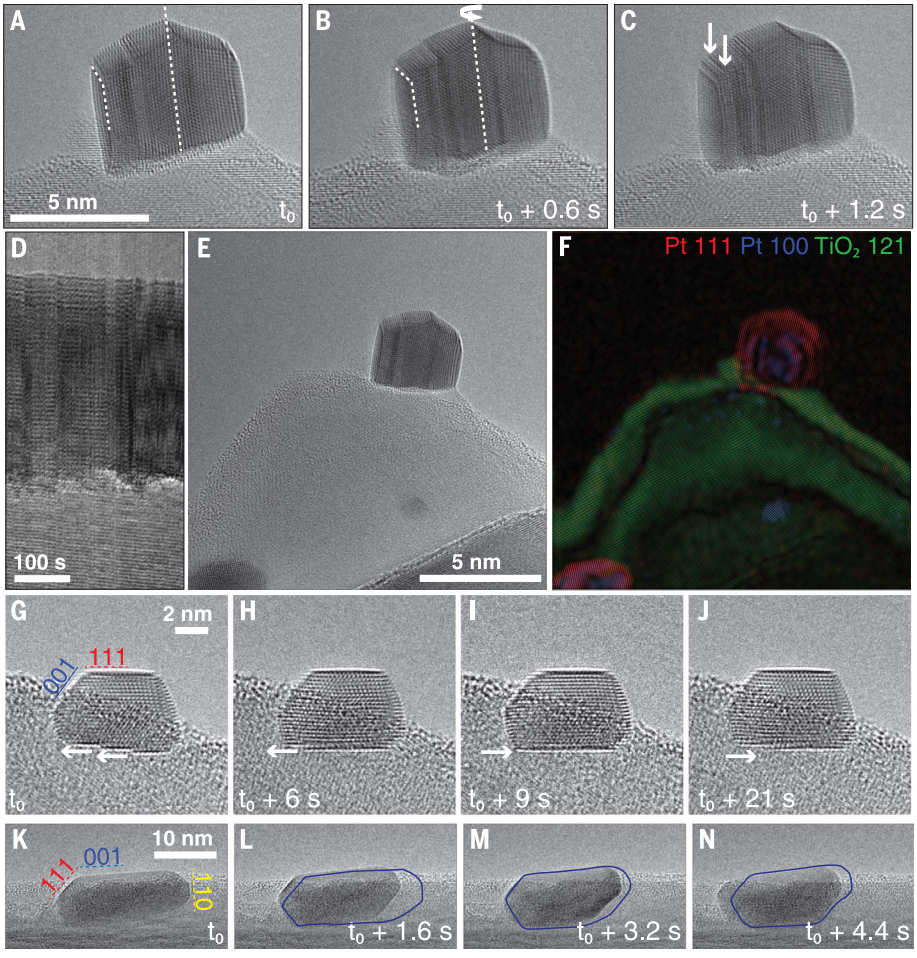

Fig. 2. Redox chemistry at the interface induces structural dynamics of Pt NPs and is the driving force for particle reconstruction and migration. (**A** to **C**) Individual frames of a movie recorded from a Pt NP that is oriented with (111) planes perpendicular to the interface. (**D**) View generated from the same movie by cutting a plane through the image stack along the time axis. It shows the up- and downward shifting of Pt(111) planes and the associated collapse and reconstruction of the underlaying TiO_2. (**E** and **F**) Image and its Fourier-filtered counterpart in which planes of identical orientation appear in the same color: Green indicates (121) planes of TiO_2 and red and blue indicate Pt(111) and Pt(100) planes, respectively. (**G** to **I**) Image sequence of a particle that is seemingly oriented with the Pt planes parallel to the TiO_2 interface. (**K** to **N**) NP that has its Pt{111} planes inclined toward the interface. The blue shapes indicate the respective positions of the Pt NP in the previous frames.

Retraction of H_2 and reformation of the oxidic SMSI overlayer

When we switched the gas composition back from a reactive to a purely oxidizing regime by turning off the H_2 flow, an encapsulated state of Pt NPs was reestablished. The first apparent effect of a reduced H_2 concentration was a sudden morphological change of the Pt NPs toward a more spherical shape, typical for the effect of O_2 (*33*) (see Fig. 3, A to C, and movie S7). Subsequently, the migration of support material onto the Pt NPs, and thus reformation of the overgrowth layer, was observed. The image sequence in Fig. 3, D to F, showed that NP coverage started at the Pt–TiO_2 interface and propagated upward. The support underneath showed a weakening of image contrast in the vicinity of the Pt NP (see Fig. 3D), indicating that the material forming the overlayer originated from there. Electron energy loss spectroscopy measurements confirmed that the overlayer consisted of TiO_2 (fig. S5).

Once the coverage was restored, all of the dynamical effects ceased, and the system reached a static state. Because water was formed as reaction product and could influence the above-described particle dynamics, further experiments were performed in which water vapor was co-fed first to an O_2-containing atmosphere [up to a partial pressure of water vapor (p_{H_2O}) ~20 mbar; supporting materials and methods] and subsequently to a mixture of O_2 (700 mbar) and H_2 (120 mbar) at 600°C. Movie S8 showed that neither particle dynamics nor migration was observed as a consequence of the added water vapor. Only after retracting water from the feed gas did particle dynamics reemerge (movie S8 and fig. S6).

Discussion

This work was motivated by questions regarding the relevance of the classical SMSI state

beyond reductive activation and thus the behavior of the system under reactive conditions. Encapsulation is often used to explain the altered behavior of supported metal NPs, although it represents a state obtained after HTR or, as recently shown, treatment in O_2. Little is known about the SMSI state under reaction conditions and its relation to catalytic function.

Starting with encapsulated NPs in an oxidizing atmosphere, the key finding of this work is that exposure to a redox-active environment led to the removal of the overlayer and subsequently the emergence of particle dynamics. Thus, the classical SMSI state was lost as soon as the surface was exposed to a reactive atmosphere. The absence of an overlayer indicated that neither the reduced TiO_2 overlayer found in H_2 nor the oxidized version found in O_2 was stable under redox conditions. The simultaneous presence of reducing and oxidizing agents induced redox processes that lead to destabilization and overlayer retraction. Hydrogen is easily activated on platinum, but activation on TiO_2 is much more unlikely (*53*–*55*). Its addition to the feed gas triggered oxygen abstraction from the overlayer, thereby destabilizing and finally stripping it from the particle surface.

The areal increase of Pt{100} facets upon overlayer retraction suggested that H_2, despite a presumably low equilibrium coverage at 600°C and 60 mbar (*56*), dominated the NP shape. Indirect evidence for activation of H_2 on Pt is provided by Fig. 1, G to I, and in movie S2, in which overlayer retraction was initiated at a kink in the NP and propagated from there across the Pt surface. A similar mechanism was observed for the reduction of an O-Fe-O trilayer on an extended Pt{111} surface during CO oxidation (*57*).

Redox-induced processes not only destabilized the encapsulating layer but also acted at the remaining Pt–TiO_2 interface and led to pronounced particle dynamics. Structural incoherence of Pt and TiO_2 (*58*) created inhomogeneous strain at the NP-support interface (*59*). The strain was modulated with a periodicity of the moiré or coincidence lattice (*60*). Strain modulation locally reduced the energetic costs for oxygen vacancy formation in the reducible support (*60*, *61*). Experimentally, similar strain-facilitated introduction of oxygen vacancies at the NP-support interface under reducing conditions was observed for a cerium oxide–rhodium model catalyst (*60*) and a gold ceria interface (*62*), and furthermore was predicted by density functional theory (DFT) for Pt on TiO_2 (*63*).

In rutile, aggregation of oxygen vacancies is energetically favored and leads to shear plane formation. These so-called Wadsley defects (*64*–*68*) can form already at low oxygen deficiencies (*69*). The introduction of shear planes reduces the elastic energy density stored in the interface (*59*) and prompts a morphology adaptation of the supported particle. With increasing extent of reduction, the local affinity of TiO_x toward reoxidation increases (*70*) up to the point at which reoxidation takes place and induces, once again, morphological adaptation of the Pt NPs. This redox-mediated reconstruction can be seen in movie S4, which shows the periodic collapse and rebuilding of the TiO_2 structure underneath a Pt NP. In a simplified model, the process can be viewed as an oscillator in which energy is transferred back and forth between strain or misfit and chemical energy. The process is driven by competing actions of H_2 and O_2 and enabled by a sufficiently high temperature and chemical potential of the constituent gases. Such atmosphere-induced reconstructions have been revealed by high-resolution transmission electron microscopy (HRTEM) in dilute atmospheres and were reported for the case of gold on gamma-iron oxide, gold on TiO_2, Au on CeO_2, and Pt on Fe_3O_4 (*37*, *43*, *71*, *72*). In all of these cases, a change in interface configuration, expressed as either a rotational movement of the particle relative to the interface (*43*) or a stepwise translational motion (*37*), was detected.

Our work bridges the pressure gap from the low-pressure, quasistatic regime to a regime in which the chemical potential of the involved species (H_2 and O_2) is sufficient to induce more substantial redox dynamics. At the applied pressure, activated hydrogen can easily remove oxygen from the underlying TiO_2 support (*53*). Overall, this process resembles the Mars van Krevelen mechanism, as oxygen from the catalyst ends up in the product (*73*). However, it is not restricted to surface reduction and oxidation. Our in situ observations show that, depending on the relative orientation of particle and support, interfacial reconstructions result in different particle dynamics. The three representative cases presented here show that interface reconstructions promoted the formation of twin boundaries and step-flow growth and retraction at Pt{111} gliding planes and can give rise to directional surface migration of Pt NPs. Under redox conditions, particle dynamics and surface migration are thus largely driven by chemical processes and determined by orientation relationships, surface structure, and topology. In this way, the migration behavior of particles can be rationalized.

The oscillatory behavior that we observed reflected the bistability associated with redox processes and the inability of the system to settle as long as a reactive state was maintained. Water, when present in excess, did not induce any dynamics, but rather quenched them. Water preferably dissociates at oxygen vacancies (*74*) and, when added in excess, worked against TiO_2 reduction by shifting the redox regime to higher temperatures. When the feed is switched back to dry H_2 plus O_2, particle dynamics re-emerged until finally, the dynamics were stopped when H_2 was removed from the feed. At that moment, a static

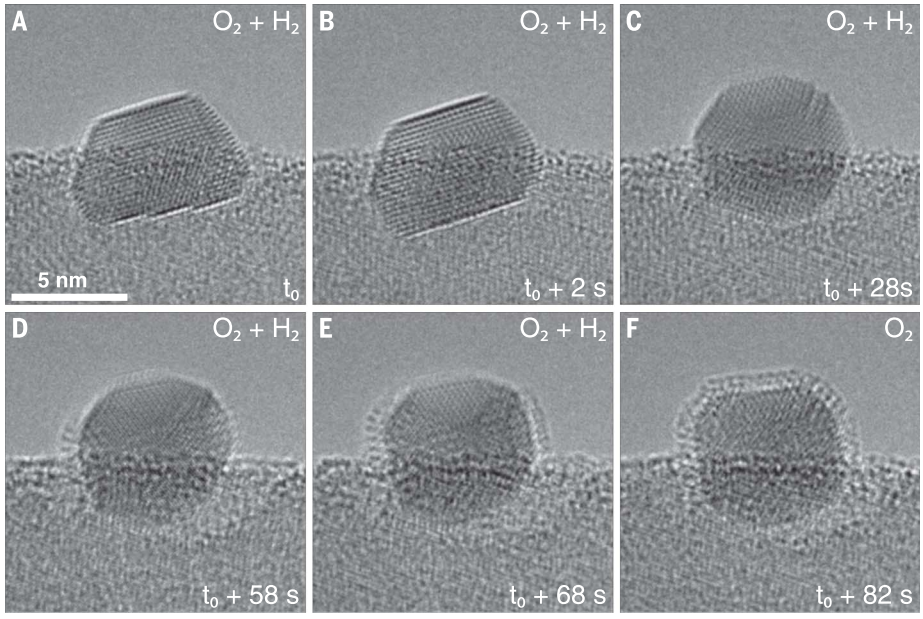

Fig. 3. Morphological change of a Pt NP upon leaving the redox-active regime. Switching of the gas atmosphere from 60 mbar H_2 plus 700 mbar O_2 back to 700 mbar O_2 at 600°C leads to reformation of a classical particle overgrowth. (**A** to **C**) The NP first adopted a spherical morphology. (**D** to **F**) As soon as H_2 was fully removed from the reactor cell, the overlayer reformed from support material from the vicinity of the NP; t_0 is the time at which the H_2 flow was set to zero.

overlayer reformed. The system thus equilibrated by reverting to an oxygen-induced SMSI state, which was formed in this case directly, without prior initialization through the well-known high-temperature reduction route. This nonclassical, oxygen-induced SMSI state was recently observed by Tang *et al.* (*20*).

The dynamic behavior described in this work remains unnoticed in ex situ and postmortem studies, highlighting the importance of in situ observations. The complex interplay between metal and support under reaction conditions that was described here for the model reaction of H_2 oxidation shows how synergistic interactions emerge at strained interfaces between metals and reducible supports and provide a means for lowering oxidation barriers. Because these effects are influenced by the local structure of the interface of each individual particle, those insights are even hidden for integral in situ methods that average over a large fraction of a sample. The reported individual behavior and its correlation to structure have to be included in models that aim to describe the overall structural transformations of a catalyst under redox conditions. Theory may then provide insight into how the dynamic behavior and interfacial redox processes lead to the formation and disappearance of active sites that link the restructuring and motion directly to the reaction kinetics.

REFERENCES AND NOTES

1. M. Haruta, *Catal. Today* **36**, 153–166 (1997).
2. T. W. van Deelen, C. Hernández Mejía, K. P. de Jong, *Nat. Catal.* **2**, 955–970 (2019).
3. S. J. Tauster, S. C. Fung, R. L. Garten, *J. Am. Chem. Soc.* **100**, 170–175 (1978).
4. A. Beck *et al.*, *Nat. Commun.* **11**, 3220 (2020).
5. W. Zhao *et al.*, *J. Phys. Chem. C* **125**, 10386–10396 (2021).
6. X. Wang, A. Beck, J. A. van Bokhoven, D. Palagin, *J. Mater. Chem. A Mater. Energy Sustain.* **9**, 4044–4054 (2021).
7. D. N. Belton, Y. M. Sun, J. M. White, *J. Phys. Chem.* **88**, 1690–1695 (1984).
8. C. S. Ko, R. J. Gorte, *J. Catal.* **90**, 59–64 (1984).
9. R. A. Demmin, C. S. Ko, R. J. Gorte, *J. Phys. Chem.* **89**, 1151–1154 (1985).
10. S. Bernal *et al.*, *J. Chem. Soc., Faraday Trans.* **92**, 2799–2809 (1996).
11. S. Zhang *et al.*, *Nano Lett.* **16**, 4528–4534 (2016).
12. J. Lee *et al.*, *J. Catal.* **330**, 19–27 (2015).
13. D. Liu *et al.*, *J. Catal.* **266**, 380–390 (2009).
14. J. Li *et al.*, *ACS Catal.* **9**, 6342–6348 (2019).
15. X. Liu *et al.*, *J. Am. Chem. Soc.* **134**, 10251–10258 (2012).
16. T. Lunkenbein, J. Schumann, M. Behrens, R. Schlögl, M. G. Willinger, *Angew. Chem.* **127**, 4627–4631 (2015).
17. H. Tang *et al.*, *Chem. Sci.* **9**, 6679–6684 (2018).
18. S. Liu *et al.*, *Nat. Commun.* **10**, 5790 (2019).
19. S. Liu *et al.*, *ACS Catal.* **11**, 6081–6090 (2021).
20. M. Tang *et al.*, *Angew. Chem. Int. Ed.* **60**, 22339–22344 (2021).
21. H. Tang *et al.*, *J. Am. Chem. Soc.* **138**, 56–59 (2016).
22. H. Tang *et al.*, *Angew. Chem. Int. Ed.* **55**, 10606–10611 (2016).
23. A. K. Datye, M. Votsmeier, *Nat. Mater.* **20**, 1049–1059 (2021).
24. G. L. Haller, D. E. Resasco, in *Advances in Catalysis* (Elsevier, 1989), vol. 36, pp. 173–235; https://linkinghub.elsevier.com/retrieve/pii/S0360056408600188.
25. A. Corma, P. Serna, P. Concepción, J. J. Calvino, *J. Am. Chem. Soc.* **130**, 8748–8753 (2008).
26. J. C. Matsubu *et al.*, *Nat. Chem.* **9**, 120–127 (2017).
27. R. M. Kennedy *et al.*, *Catal. Lett.* **148**, 2223–2232 (2018).
28. M. Macino *et al.*, *Nat. Catal.* **2**, 873–881 (2019).
29. M. G. Willinger *et al.*, *Angew. Chem. Int. Ed.* **53**, 5998–6001 (2014).
30. S. Shaikhutdinov, *Catal. Lett.* **148**, 2627–2635 (2018).
31. O. Dulub, W. Hebenstreit, U. Diebold, *Phys. Rev. Lett.* **84**, 3646–3649 (2000).
32. P. L. Hansen *et al.*, *Science* **295**, 2053–2055 (2002).
33. T. Altantzis *et al.*, *Nano Lett.* **19**, 477–481 (2019).
34. H. Yoshida *et al.*, *Appl. Phys. Express* **4**, 065001 (2011).
35. Y. Kuwauchi, H. Yoshida, T. Akita, M. Haruta, S. Takeda, *Angew. Chem. Int. Ed.* **51**, 7729–7733 (2012).
36. T. W. Hansen *et al.*, *Science* **294**, 1508–1510 (2001).
37. Y. Kuwauchi *et al.*, *Nano Lett.* **13**, 3073–3077 (2013).
38. Y. Li *et al.*, *Nat. Commun.* **12**, 914 (2021).
39. J. B. Wagner, F. Cavalca, C. D. Damsgaard, L. D. L. Duchstein, T. W. Hansen, *Micron* **43**, 1169–1175 (2012).
40. M. Plodinec *et al.*, *Microsc. Microanal.* **26**, 220–228 (2020).
41. M. Boniface, M. Plodinec, R. Schlögl, T. Lunkenbein, *Top. Catal.* **63**, 1623–1643 (2020).
42. A. Beck *et al.*, *Nat. Catal.* **4**, 488–497 (2021).
43. W. Yuan *et al.*, *Science* **371**, 517–521 (2021).
44. J. Vincent, P. Crozier, *Microsc. Microanal.* **26** (S2), 1694–1695 (2020).
45. A. Akram *et al.*, *Chem. Sci.* **7**, 5833–5837 (2016).
46. M. Chi *et al.*, *Nat. Commun.* **6**, 8925 (2015).
47. J. Resasco, S. Dai, G. Graham, X. Pan, P. Christopher, *J. Phys. Chem. C* **122**, 25143–25157 (2018).
48. X. Du, H. Tang, B. Qiao, *Catalysts* **11**, 896 (2021).
49. R. Vanselow, M. Mundschau, *J. Catal.* **103**, 426–435 (1987).
50. X. Xu, Q. Fu, L. Gan, J. Zhu, X. Bao, *J. Phys. Chem. B* **122**, 984–990 (2018).
51. U. Diebold, *Surf. Sci. Rep.* **48**, 53–229 (2003).
52. T. Kandemir *et al.*, *Angew. Chem. Int. Ed.* **52**, 5166–5170 (2013).
53. A. Beck *et al.*, *J. Phys. Chem. C* **125**, 22531–22538 (2021).
54. J. M. Herrmann, M. Gravelle-Rumeau-Maillot, P. C. Gravelle, *J. Catal.* **104**, 136–146 (1987).
55. G. B. Raupp, J. A. Dumesic, *J. Phys. Chem.* **89**, 5240–5246 (1985).
56. C. Spreafico, W. Karim, Y. Ekinci, J. A. van Bokhoven, J. VandeVondele, *J. Phys. Chem. C* **121**, 17862–17872 (2017).
57. K. Zhang, L. Li, S. Shaikhutdinov, H.-J. J. Freund, *Angew. Chem. Int. Ed.* **57**, 1261–1265 (2018).
58. A. J. Fox, B. Drawl, G. R. Fox, B. J. Gibbons, S. Trolier-McKinstry, *IEEE Trans. Ultrason. Ferroelectr. Freq. Control* **62**, 56–61 (2015).
59. P. Müller, R. Kern, *Surf. Sci.* **457**, 229–253 (2000).
60. C. Castellarin-Cudia *et al.*, *Surf. Sci.* **554**, L120–L126 (2004).
61. A. Ruiz Puigdollers, P. Schlexer, S. Tosoni, G. Pacchioni, *ACS Catal.* **7**, 6493–6513 (2017).
62. J. L. Vincent, P. A. Crozier, *Microsc. Microanal.* **25** (S2), 1508–1509 (2019).
63. S. C. Ammal, A. Heyden, *J. Chem. Phys.* **133**, 164703 (2010).
64. C. Bäumer, R. Dittmann, in *Metal Oxide-Based Thin Film Structures* (Elsevier, 2018), pp. 489–522; https://linkinghub.elsevier.com/retrieve/pii/B9780128111666000200.
65. R. J. Kamaladasa *et al.*, *Microsc. Microanal.* **21**, 140–153 (2015).
66. D. S. Jeong, H. Schroeder, U. Breuer, R. Waser, *J. Appl. Phys.* **104**, 123716 (2008).
67. L. A. Bursill, B. G. Hyde, *Philos. Mag.* **23**, 3–15 (1971).
68. L. A. Bursill, B. G. Hyde, D. K. Philp, *Philos. Mag.* **23**, 1501–1513 (1971).
69. B. F. Donovan *et al.*, *Acta Mater.* **127**, 491–497 (2017).
70. M. D. Rasmussen, L. M. Molina, B. Hammer, *J. Chem. Phys.* **120**, 988–997 (2004).
71. P. Liu *et al.*, *Nanoscale* **11**, 11885–11891 (2019).
72. W. Gao, Z. D. Hood, M. Chi, *Acc. Chem. Res.* **50**, 787–795 (2017).
73. P. Mars, D. W. van Krevelen, *Chem. Eng. Sci.* **3**, 41–59 (1954).
74. R. Schaub *et al.*, *Phys. Rev. Lett.* **87**, 266104 (2001).

ACKNOWLEDGMENTS

Funding: H.F. and M.G.W. acknowledge the SNSF project 200021_181053; A.B. and J.A.vB. acknowledge the SNSF project 200021_178943. **Author contributions:** Conceptualization: M.G.W.; Investigation: H.F., A.B., X.H., and M.G.W.; Visualization: H.F. and M.G.W.; Funding acquisition: M.G.W.; Project administration: M.G.W. and J.A.vB.; Supervision: M.G.W., X.H., and J.A.vB.; Writing—original draft: H.F. and M.G.W.; Writing—review and editing: M.G.W., H.F., A.B., X.H., and J.A.vB. **Competing interests:** The authors declare that they have no competing interests. **Data and materials availability:** All data are available in the main text or the supplementary materials; additional details can be requested from the corresponding authors. Further high-resolution data are stored in the public data repository of ETH Zürich under https://www.research-collection.ethz.ch/handle/20.500.11850/546680. **License information:** This research was funded in whole or in part by SNSF project 200021_181053 and 200021_178943, a cOAlition S organization. The author will make the Author Accepted Manuscript (AAM) version available under a CC BY public copyright license.

SUPPLEMENTARY MATERIALS

science.org/doi/10.1126/science.abm3371
Materials and Methods
Figs. S1 to S6
References (*75*, *76*)
Movies S1 to S8

Submitted 14 September 2021; resubmitted 1 March 2022
Accepted 20 April 2022
10.1126/science.abm3371